Solid-State Batteries

Influence of Iron Sulfide Nanoparticle Sizes in Solid-State Batteries**

Georg F. Dewald, Zainab Liaqat, Martin Alexander Lange, Wolfgang Tremel, and Wolfgang G. Zeier*

Abstract: *Given the inherent performance limitations of intercalation-based lithium-ion batteries, solid-state conversion batteries are promising systems for future energy storage. A high specific capacity and natural abundancy make iron disulfide (FeS$_2$) a promising cathode-active material. In this work, FeS$_2$ nanoparticles were prepared solvothermally. By adjusting the synthesis conditions, samples with average particle diameters between 10 nm and 35 nm were synthesized. The electrochemical performance was evaluated in solid-state cells with a Li-argyrodite solid electrolyte. While the reduction of FeS$_2$ was found to be irreversible in the initial discharge, a stable cycling of the reduced species was observed subsequently. A positive effect of smaller particle dimensions on FeS$_2$ utilization was identified, which can be attributed to a higher interfacial contact area and shortened diffusion pathways inside the FeS$_2$ particles. These results highlight the general importance of morphological design to exploit the promising theoretical capacity of conversion electrodes in solid-state batteries.*

Iron disulfide FeS$_2$ has been explored as a high-energy, abundant and environmentally friendly material for electrochemical energy storage.[1–3] While Li-FeS$_2$ primary batteries are commercially available, the poor reversibility has limited the application of rechargeable cells. Compared to intercalation-type active materials, conversion reactions of transition metal sulfides often suffer from limited reversibility due to sluggish kinetics, detrimental volume changes and the often insulating character of reaction products.[4–6] With the goal of enabling the reversible four-electron energy storage in FeS$_2$-based cathodes nanostructuring of active materials seems promising.[7,8] In Li-FeS$_2$ cells, the influence of the FeS$_2$ crystallite size on the cell performance has been studied in the past with both liquid and solid electrolytes as slow lithium diffusion within FeS$_2$ results in kinetic limitations.[9–11] By improving the reaction kinetics and lowering the needed Li$^+$ diffusion pathways with reduced particle sizes, the reversibility and rate capability has been improved.[12,13]

Nevertheless, similar to Li-S batteries, the detrimental dissolution of polysulfides is possible in Li-FeS$_2$ batteries,[14,15] and a potential mitigation strategy could be the use in solid-state batteries.[16] Whereas sulfide-based solid electrolytes suffer from oxidative decomposition in contact to high-voltage intercalation electrodes, the lower redox potential of FeS$_2$ possibly better agrees with the oxidative stability limit of thiophosphates.[17–19] This constitutes an additional advantage for using FeS$_2$ as a cathode active material.

Thus, inspired by the promising option of tailoring the particle sizes of FeS$_2$ and their potential use in solid-state batteries, in this work we prepared FeS$_2$ nanoparticles with various size distributions and characterized their electrochemical performance in solid-state batteries. Reduced FeS$_2$ nanoparticle sizes showed a positive impact on the total capacity and rate capability, highlighting the potential of nanosized FeS$_2$ as cathode active conversion material in solid-state batteries.

The FeS$_2$ nanoparticles were prepared solvothermally and all experimental details can be found in the Supporting Information. Figure 1a shows the X-ray diffraction patterns of the as-obtained FeS$_2$ samples in which all intensities can be assigned to cubic FeS$_2$ without detectable crystalline impurities. By varying the ratio of oleic acid (OAc) to oleylamin (OAm), denoted as OAc:OAm, different particle size distributions were obtained. The different average particle sizes are evaluated using a Pawley fit (see Supporting Information),[20] and three different average particle sizes of 11($\pm$0.3) nm, 33($\pm$0.3) nm and 36($\pm$0.5) nm are found. Transmission electron microscopy (TEM) was used to evaluate the particle size distribution (Figure 1b,c). For reasonable statistics, around 100 particles of a representative sample section were analyzed. Particle diameters were calculated by assuming an ideal spherical particle shape based on the measured area. For the FeS$_2$ samples in this study, a decreased OAc:OAm ratio was found to result in reduced particles sized. Consequently, the smallest particles in the range of 5–15 nm were found for an OAc:OAm ratio of 1:2. Overall, average particle sizes of 9.7($\pm$1.3) nm, 22.1($\pm$1.5) nm and

[*] Dr. G. F. Dewald
Institute of Physical Chemistry, Justus-Liebig-University Giessen
Heinrich-Buff-Ring 17, 35392 Giessen (Germany)

Z. Liaqat, M. A. Lange, Prof. Dr. W. Tremel
Chemistry Department, Johannes Gutenberg University
Duesbergweg 10–14, 55128 Mainz (Germany)
E-mail: tremel@uni-mainz.de

Prof. Dr. W. G. Zeier
Institute of Inorganic and Analytical Chemistry, University of Münster
Corrensstrasse 30, 48149 Münster (Germany)
and
Helmholtz Insitut Münster, FZ Jülich
Corensstrasse 46, 48149 Münster (Germany)
E-mail: wzeier@uni-muenster.de

[**] A previous version of this manuscript has been deposited on a preprint server (https://doi.org/10.26434/chemrxiv.14483370).

Supporting information and the ORCID identification number(s) for the author(s) of this article can be found under: https://doi.org/10.1002/anie.202106018.
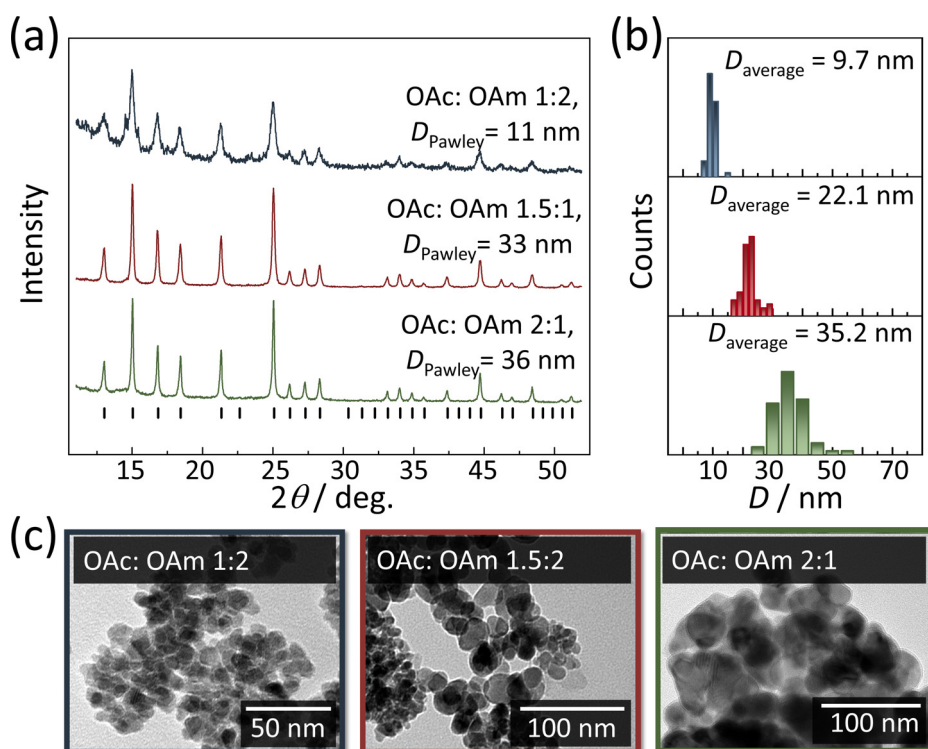
Figure 1. (a) X-ray diffractograms of FeS$_2$ nanoparticles from solvothermal reactions as a function of oleic acid (OAc): oleylamine (OAm) ratios: 1:2 (blue), 1.5:1 (red) and 2:1 (green), recorded with Mo K$_\alpha$ radiation. Average particle sizes are estimated and shown as insets based on Pawley fitting. (b) Particle size distributions of as-synthesized FeS$_2$ particles from TEM imaging. (c) TEM images of the as-synthesized FeS$_2$ particles. For an OAc:OAm ratio of 1:2, particle sizes were in the range of 5–15 nm, OAc:OAm ratios of 1.5:1 and 2:1 resulted in larger particles.

35.2($\pm$4.9) nm are found via TEM, which corroborate the sizes obtained from X-ray diffraction.

Solid-state In/InLi | Li$_6$PS$_5$Cl | FeS$_2$-Li$_6$PS$_5$Cl-C cells were assembled to evaluate the influence of the FeS$_2$ nanoparticle sizes on the resulting electrochemical properties. Cathodes were prepared with a FeS$_2$ loading of 3.8 mg cm^{-2}. In order to ensure sufficient ionic and electronic charge transport within
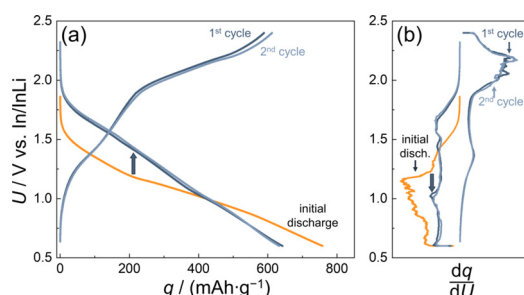

Figure 2. Typical potential profiles of initial discharge (orange) and the subsequent cycles (blue) of InLi/Li$_6$PS$_5$Cl/FeS$_2$-C- Li$_6$PS$_5$Cl cell with an average FeS$_2$ particle size $\bar{D}$ of 9.7 nm. The initial discharge is characterized by two slopes and a high capacity of 760 mAh g^{-1}. Two processes are observed for the following charging. However, the subsequent discharge steps differ significantly from the initial reduction of FeS$_2$. Besides cycling of FeS$_2$ and associated phases, reductive/oxidative decomposition of Li$_6$PS$_5$Cl and cycling of decomposed phases are expected in this potential range.

the cathodes, high volume fractions of carbon and solid electrolyte (23 vol% C, 63 vol% Li$_6$PS$_5$Cl) were employed.[21] Unlike conventional layered oxide cathode materials, FeS$_2$ is discharged in the initial cyclization step. The subsequent charge-discharge cycle is defined as first cycle in the following.

Figure 2 shows the potential profile for the initial discharge and the following charge-discharge cycles of an exemplary cell. The initial discharge differs from the subsequent steps. During the initial discharge, two slopes indicate that different reduction reactions are occurring. Accordingly, two slopes are observed in the following first charge. Importantly, the high initial discharge capacity of 760 mAh g^{-1} cannot be recovered during charging. Comparing initial and first discharge, the latter is characterized by significantly higher potentials and a lower overall capacity. Based on this complex behavior, the underlying cell reactions are likely highly convoluted. The overall four-electron reduction of FeS$_2$ during the initial discharge is typically described by [Eq. (1)]

$$FeS_2 + 4 Li^+ + 4 e^- \rightarrow 2 Li_2S + Fe, \tag{1}$$
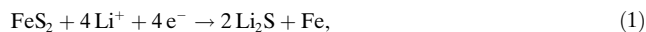
corresponding to a theoretical specific capacity of 894 mAh g^{-1}. As the initial discharge capacity is close to this value, contributions of both Fe^{+II} and S^{-I} reduction are expected here. Commonly, a two-step reaction via reduction of FeS$_2$ to Li$_2$FeS$_2$ followed by reduction to Fe^0 and Li$_2$S, is assumed.[22,23] During charging, the formation of multiple electrochemically active species, for instance S, FeS$_y$ and Li$_x$FeS$_2$, was reported before and may be at play here, especially since the significant difference between initial and first discharge is observed.[24,25] Yersak et al. attributed the irreversibility of the initial discharge to the formation of orthorhombic FeS$_2$ during the first charge,[9] but formation of Fe^0 can also be expected to lead to irreversibility. Additionally, volume changes of the active material during cycling need to be considered together with chemomechanical degradation.[26] Furthermore, reductive decomposition of the electrolyte Li$_6$PS$_5$Cl may be expected during the initial discharge,[18,27] and a certain additional capacity from the solid electrolyte seems possible.[19] However, the decomposition of the solid electrolyte seems negligible, considering the minor changes in the X-ray photoemission spectra (see below). Consequently, the irreversible capacity of the initial discharge

is most likely caused by a superposition of the partial irreversible reduction of FeS_2, electrochemical electrolyte degradation and chemomechanical losses. Overall, a resulting complex mixture of multiple redox-active species during the initial discharge and the following charge seems to occur in FeS_2 based solid state batteries.

By comparing the electrochemical performance of FeS_2-Li_6PS_5Cl cathodes, the influence of FeS_2 particle size on the electrochemical utilization is highlighted (Figure 3). While the potential profiles show similar characteristics for all investigated samples, the overall capacity as well as the performance at higher cycling rates is improved by reduced particle sizes, despite the slightly higher overall cell resistances (see Supporting Information S5). Within the investigated period of 40 cycles, continuous capacity fading is observed, which is stressed for the sample with the smallest particles. This trend can possibly be explained by the higher interfacial area between FeS_2 and conducting cathode matrix for smaller particles.

In order to elucidate the underlying processes and differences of different particle sizes during cyclization in FeS_2-C-Li_6PS_5Cl cathode composites, the composites were character-
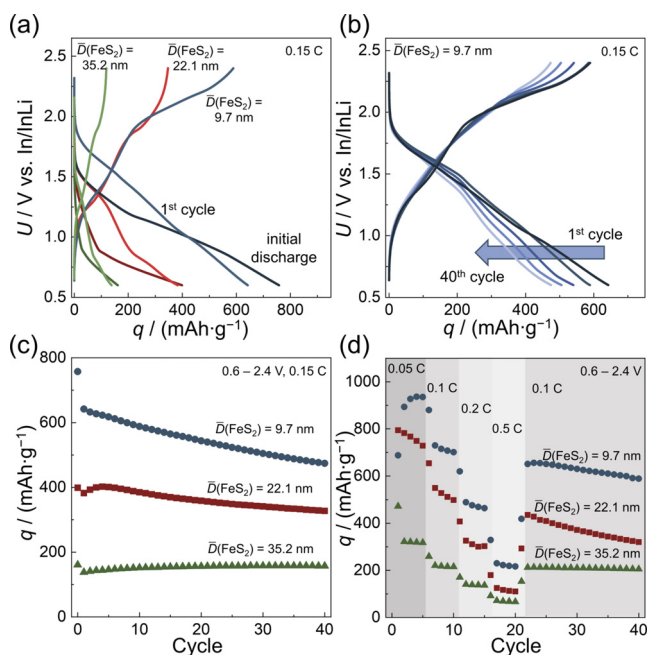
Figure 3. Influence of the FeS_2 particle size on performance of In/InLi | Li_6PS_5Cl | FeS_2-C-Li_6PS_5Cl cells at 25 °C and an areal FeS_2 loading of 3.8 mg cm^{-2} in the cathode composite. C-rates were calculated based on four electron reductions of FeS_2 (0.1 C = 340 μA cm^{-2}). While similar characteristics regarding the irreversibility of the initial discharge are observed in U-q plots, larger FeS_2 particles lead to lower capacities in the initial discharge and following first cycle (a). Despite the irreversible reduction of FeS_2 in the initial discharge, long-term cyclization performance suffers only from a gradual capacity fade over 40 cycles, shown exemplary for the cell with an average FeS_2 nanoparticle size of 9.7 nm (b). In direct comparison of long-term cyclization performance, the highest discharge capacities are obtained for a FeS_2 particle size of 9.7 nm (c). A similar trend is found for cyclization at different rates (d). Impedance spectra of the cells shown in (a) and (c) recorded prior to cycling can be found in the Supporting Information.

ized *post-mortem* by X-ray photoelectron spectroscopy (XPS). All the S 2p and P2 p spectra for the Li_6PS_5Cl can be found in the Supporting Information. Most likely due to a low overall atomic fraction of Fe in the investigated cathode composites (approx. 5 at.-%), the Fe spectra cannot be resolved. Figure 4 shows S 2p detail spectra of the pristine FeS_2 particles as well as the cathode composites at different charged and discharged states during cyclization. Besides the expected S_2^{2-} main contribution at around 162.5 eV, both reduced and oxidized sulfur species appear. A broad peak ($E(2p_{3/2}) = 163.6$ eV) can be correlated to the presence of sulfur and long-chain sulfides. Additionally, peaks at higher binding energies (167–169 eV) are found for all samples, which can be assigned to sulfate (SO_4^{2-}) and sulfite (SO_3^{2-}) species.[28,29] A reduced species ($E(2p_{3/2}) = 161.4$ eV) can be attributed to sulfide ions (S^{2-}), possibly due to FeS as side product.[22,30] These contributions cannot be fully deconvoluted due to peak overlap. Sulfate and sulfite species have been identified by XPS analyses on solvothermally synthesized FeS_2 before and were attributed to surface species.[31] Therefore, these additional phases may just be part of the spectra due to the high surface sensitivity of XPS and the high surface to bulk ratio of the FeS_2 nanoparticles. After adding the solid electrolyte Li_6PS_5Cl, the contributions of FeS_2 and the solid electrolyte in the resulting cathode composite are strongly convoluted. The S 2p detail spectrum of pristine Li_6PS_5Cl shows a main contribution at 161.6 eV of the PS_4^{3-} tetrahedra as well as the free S^{2-} anion at 160.0 eV. While small differences in binding energies impede the resolution of the individual sulfur contributions (S_2^{2-} in FeS_2, S^{2-} and PS_4^{3-} in Li_6PS_5Cl), significant changes in S 2p spectra indicate different sulfur oxidation states in the discharged and charged samples. A clear increase in intensity of the reduced sulfur species S^{2-} can be found after the initial cell discharge. During the subsequent charge, (partial) re-oxidation shows the contribution of sulfur to the cell capacity as the S^{2-} signal decreases again. In comparison between cathodes with varied FeS_2 particle sizes, less severe changes upon cyclization are observed in the S 2p spectra for larger FeS_2 particle sizes (Figure 4b). The lower intensity of the reduction to S^{2-} for the larger average particle sizes is in accordance with the lower capacity observed during cycling and can be interpreted as hindered active material utilization for larger FeS_2 particle sizes.

While the exact deconvolution of contributions here is difficult, due to the superposition of FeS_2, Li_6PS_5Cl and possible other decomposition products, certain information can be inferred. During the initial discharge, the $(S_2)^{2-}$ in FeS_2 will mostly be reduced to Fe^0 and S^{2-}, forming Li_2S, while reduction of P^{5+} would result in the decomposition of crystalline Li_6PS_5Cl as recently observed.[18,27] In the following charge, oxidation of Li_2S as well as possible Fe must be expected to result in the observed multiple redox-active phases. In Li-FeS_2 cells, Fong and Dahn suggested that FeS_2, FeS_y and S are formed during charging.[24] For the oxidative conditions, decomposition of Li_6PS_5Cl to S, P_2S_5 and LiCl was predicted theoretically.[32] However, considering the P 2p spectra of the cycled FeS_2-Li_6PS_5Cl-C cathodes, minor changes are found that suggest that the dominant electro-
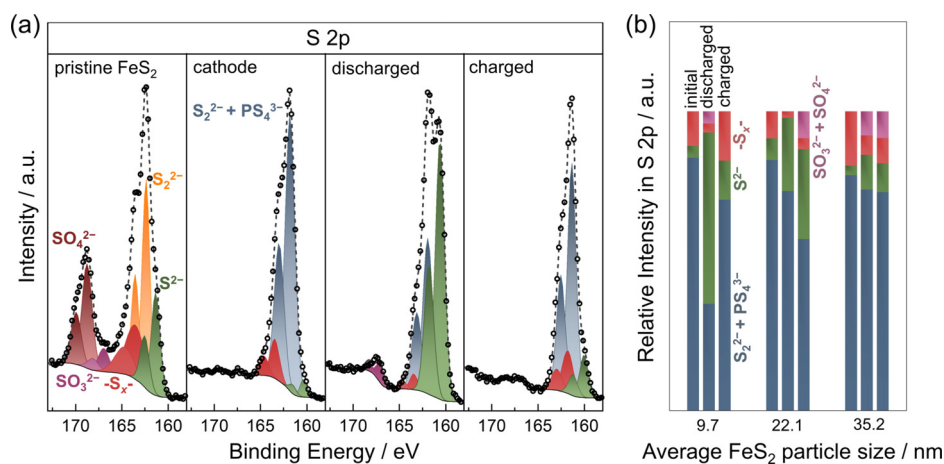
Figure 4. X-ray photoemission sulfur detail spectra of pristine FeS$_2$ nanoparticles (average particle sizes $\bar{D}$ of 9.7 nm) and FeS$_2$-C-Li$_6$PS$_5$Cl cathodes composites (a). A spectrum with multiple contributions is observed for as-synthesized FeS$_2$ particles. After addition of carbon black and Li$_6$PS$_5$Cl, the solid electrolyte and FeS$_2$ contributions to the sulfur signal overlap. An increasing intensity of reduced species indicates sulfur reduction upon cell discharge, reoxidized in the subsequent charge. By visualizing the changes in relative intensity contributions to the S 2p spectra upon cycling, a clear influence of FeS$_2$ particle size on the extent of sulfur cycling is highlighted (b). Values of relative intensities in S 2p as well as P 2p detail spectra are also shown in the (Supporting Information). This trend can be interpreted as improved sulfur utilization for small FeS$_2$ particle sizes.

chemical mechanisms involve the sulfur species. This suggests a degree of oxidative solid electrolyte degradation,[17] which however seems to be independent of particle size and hence surface area of the employed FeS$_2$ particles. Therefore, the more pronounced sulfur redox behavior that can be found when using the smallest sizes FeS$_2$ nanoparticles suggests that more FeS$_2$ is electrochemically addressed and converted (see Figure 4b).

To exploit the remarkable theoretical capacity of conversion-type electrode materials in competitive solid-state batteries, performance bottlenecks such as low utilization of active materials and poor cycling efficiencies must be overcome. In this work, we used FeS$_2$ as a model-type conversion cathode for solid-state Li-ion storage due to its facile synthesis and high theoretical capacity. FeS$_2$ nanoparticles with three different size distributions were synthesized and characterized. The influence of the size distribution of FeS$_2$ on the solid-state battery performance was evaluated for In/InLi | Li$_6$PS$_5$Cl | FeS$_2$-C-Li$_6$PS$_5$Cl cells. A higher capacity and better rate capability were obtained for smaller particle sizes that are unfortunately also accompanied by faster capacity fading. The higher capacity and better rate capability is likely caused by the fact that more active material can be addressed due to the higher surface to volume ratio and the shorter Li$^+$ diffusion pathways inside the FeS$_2$ nanoparticles. Nevertheless, this higher surface to volume ratio provides more interfacial area for competing decomposition reactions and more capacity fading.

Overall, this work highlights the potential of FeS$_2$ as conversion-type cathode material and especially the high relevance of using nanoscale conversion materials in solid state batteries. It further shows that, similar to solid-state batteries with oxide-based cathode active materials,[33] par-

ticle size distribution of the cathode active materials also matters significantly in conversion-type solid-state batteries.

Conflict of Interest

The authors declare no conflict of interest.

Keywords: conversion electrodes · iron sulfide · nanoparticles · solid-state batteries

[1] E. Peled, D. Golodnitsky, E. Strauss, J. Lang, Y. Lavi, *Electrochim. Acta* **1998**, *43*, 1593–1599.

[2] Y. Shao-Horn, Q. C. Horn, *Electrochim. Acta* **2001**, *46*, 2613–2621.

[3] J. Xia, J. Jiao, B. Dai, W. Qiu, S. He, W. Qiu, P. Shen, L. Chen, *RSC Adv.* **2013**, *3*, 6132–6140.

[4] A. Kraytsberg, Y. Ein-Eli, *J. Solid State Electrochem.* **2017**, *21*, 1907–1923.

[5] S.-H. Yu, X. Feng, N. Zhang, J. Seok, H. D. Abruña, *Acc. Chem. Res.* **2018**, *51*, 273–281.

[6] A. L. Santhosha, N. Nazer, R. Koerver, S. Randau, F. H. Richter, D. A. Weber, J. Kulisch, T. Adermann, J. Janek, P. Adelhelm, *Adv. Energy Mater.* **2020**, *10*, 2002394.

[7] C. H. Lai, M. Y. Lu, L. J. Chen, *J. Mater. Chem.* **2012**, *22*, 19–30.

[8] Y. Lu, L. Yu, X. W. (David) Lou, *Chem* **2018**, *4*, 972–996.

[9] T. A. Yersak, H. A. Macpherson, S. C. Kim, V. D. Le, C. S. Kang, S. B. Son, Y. H. Kim, J. E. Trevey, K. H. Oh, C. Stoldt, S. H. Lee, *Adv. Energy Mater.* **2013**, *3*, 120–127.

[10] A. Douglas, R. Carter, L. Oakes, K. Share, A. P. Cohn, C. L. Pint, *ACS Nano* **2015**, *9*, 11156–11165.

[11] M. Walter, T. Zünd, M. V. Kovalenko, *Nanoscale* **2015**, *7*, 9158–9163.

[12] Y. Shao-Horn, S. Osmialowski, Q. C. Horn, *J. Electrochem. Soc.* **2002**, *149*, A1499.

[13] D. Zhang, J. P. Tu, J. Y. Xiang, Y. Q. Qiao, X. H. Xia, X. L. Wang, C. D. Gu, *Electrochim. Acta* **2011**, *56*, 9980–9985.

[14] S. Qi, L. Mi, K. Song, K. Yang, J. Ma, X. Feng, J. Zhang, W. Chen, *J. Phys. Chem. C* **2019**, *123*, 2775–2782.

[15] M. T. McDowell, Z. Lu, K. J. Koski, J. H. Yu, G. Zheng, Y. Cui, *Nano Lett.* **2015**, *15*, 1264–1271.

[16] J. Janek, W. G. Zeier, *Nat. Energy* **2016**, *1*, 16141.

[17] R. Koerver, F. Walther, I. Aygün, J. Sann, C. Dietrich, W. G. Zeier, J. Janek, *J. Mater. Chem. A* **2017**, *5*, 22750–22760.

[18] T. K. Schwietert, V. A. Arszelewska, C. Wang, C. Yu, A. Vasileiadis, N. J. J. de Klerk, J. Hageman, T. Hupfer, I. Kerkamm, Y. Xu, E. van der Maas, E. M. Kelder, S. Ganapathy, M. Wagemaker, *Nat. Mater.* **2020**, *19*, 428–435.

[19] G. F. Dewald, S. Ohno, M. A. Kraft, R. Koerver, P. Till, N. M. Vargas-Barbosa, J. Janek, W. G. Zeier, *Chem. Mater.* **2019**, *31*, 8328–8337.

[20] G. S. Pawley, *J. Appl. Crystallogr.* **1981**, *14*, 357–361.

[21] G. F. Dewald, S. Ohno, J. G. C. Hering, J. Janek, W. G. Zeier, *Batteries Supercaps* **2021**, *4*, 183–194.

[22] E. Strauss, D. Golodnitsky, K. Freedman, A. Milner, E. Peled, *J. Power Sources* **2003**, *115*, 323–331.

[23] S. S. Zhang, D. T. Tran, *Electrochim. Acta* **2015**, *176*, 784–789.

[24] R. Fong, J. R. Dahn, *J. Electrochem. Soc.* **1989**, *136*, 3206.

[25] U. Ulissi, S. Ito, S. M. Hosseini, A. Varzi, Y. Aihara, S. Passerini, *Adv. Energy Mater.* **2018**, *8*, 1801462.

[26] S. Ohno, R. Koerver, G. Dewald, C. Rosenbach, P. Titscher, D. Steckermeier, A. Kwade, J. Janek, W. G. Zeier, *Chem. Mater.* **2019**, *31*, 2930–2940.

[27] S. Ohno, C. Rosenbach, G. F. Dewald, J. Janek, W. G. Zeier, *Adv. Funct. Mater.* **2021**, *31*, 2010620.

[28] F. Walther, R. Koerver, T. Fuchs, S. Ohno, J. Sann, M. Rohnke, W. G. Zeier, J. Janek, *Chem. Mater.* **2019**, *31*, 3745–3755.

[29] J. Auvergniot, A. Cassel, D. Foix, V. Viallet, V. Seznec, R. Dedryvère, *Solid State Ionics* **2017**, *300*, 78–85.

[30] P. Velásquez, D. Leinen, J. Pascual, J. R. Ramos-Barrado, P. Grez, H. Gómez, R. Schrebler, R. Del Río, R. Córdova, *J. Phys. Chem. B* **2005**, *109*, 4977–4988.

[31] J. Xia, J. Jiao, B. Dai, W. Qiu, S. He, W. Qiu, P. Shen, L. Chen, *RSC Adv.* **2013**, *3*, 6132.

[32] Y. Zhu, X. He, Y. Mo, *ACS Appl. Mater. Interfaces* **2015**, *7*, 23685–23693.

[33] E. Trevisanello, R. Ruess, G. Conforto, F. H. Richter, J. Janek, *Adv. Energy Mater.* **2021**, *11*, 2003400.